

Modeling Elastic-Body Dynamics of Fish Swimming Using a Variational Framework

Zhiheng Chen and Wei Wang*

Abstract—Fish-inspired aquatic robots are gaining increasing attention in research communities due to their high swimming speeds and efficient propulsion enabled by flexible bodies that generate undulatory motions. To support the design optimizations and control of such systems, accurate, interpretable, and computationally tractable modeling of the underlying swimming dynamics is indispensable. In this letter, we present a full-body dynamics model for fish swimming, rigorously derived from Hamilton’s principle. The model captures the continuously distributed elasticity of a deformable fish body undergoing large deformations and incorporates fluid-structure coupling effects, enabling self-propelled motion without prescribing kinematics. A preliminary parameter study explores the influence of actuation frequency and body stiffness on swimming speed and cost of transport (COT). Simulation results indicate that swimming speed and energy efficiency exhibit opposing trends with tail-beat frequency and that both body stiffness and body length have distinct optimal values. These findings provide insights into biological swimming mechanisms and inform the design of high-performance soft robotic swimmers.

I. INTRODUCTION

Biomimetic swimming robots have drawn increasing interest in research communities in recent years, due to their potential for energy-efficient and agile locomotion in complex aquatic environments [1], [2]. Among these biomimetic swimmers, fish-like robots are particularly promising, since they utilize flexible bodies and undulatory motion to achieve high speed, propulsive efficiency, and maneuverability [3]–[5]. Therefore, accurate modeling of the dynamics of fish swimming is essential, not only for understanding the underlying principles of aquatic locomotion, but also for insights into the design, optimizations, and control of bio-inspired robotic swimmers.

Plenty of theoretical and computational efforts have been made to study the dynamics of fish swimming. A common approach is to model the dynamics based on multi-segment methods [6]–[12]. Most of these methods model the fish as a chain of rigid bodies, and the elasticity of the fish’s body is lumped into the joints using torsional springs; though the work in [12] adopts an elastic rod framework, the actual implementation reduces the fish body to a chain of rigid segments with locally defined bending potentials limited to the connections of segments. An exception is the model presented in [10], where an arc is used to approximate the deformation of each segment and thus adds another degree of freedom for each segment.

Although these multi-segment methods show good computational efficiencies, they struggle to capture the inherently

continuous characteristic of the deformations of fish bodies. Specifically, a real fish has a body curvature that exhibits smooth changes along its length, rather than sharp changes limited to joint locations, and thus the non-negligible discretization error introduced by multi-segment methods can lead to inaccurate representations of the wave propagations and coupled dynamics between the fish and the surrounding water. This inaccuracy can be problematic for analyzing the propulsion mechanism of fish swimming, where accurate modeling of the smooth and continuous undulatory motion is critical.

Another approach to studying fish swimming dynamics is to perform numerical simulations based on computational fluid dynamics (CFD) and fluid-structure interactions (FSI); the latter solves for both the solid and fluid fields. The FSI-based simulations presented in [13] successfully provides high-fidelity results of muscle-actuated fish swimming. A CFD-based model that accurately captures the vortex shedding during fish swimming is presented in [14]; however, the work prescribes the deformation pattern of the fish’s body, and thus does not provide a full-dynamics analysis. The work in [15] also presents an FSI-based model that provides a detailed analysis on the fluid dynamics of surrounding water and the effects of stiffness tuning on propulsion performances; however, the solid part of the model is reduced to a two-rigid-body linkage with a joint loaded by nonlinear spring and damper.

Despite their potentially outstanding accuracies, FSI and CFD models often cannot provide highly interpretable closed form equations of motion, which is of great significance for control, model reduction, and system identification tasks. Moreover, high-fidelity FSI and CFD simulations are computationally expensive, and a single simulation can take days to weeks to complete even with GPU accelerations [16], [17], which makes iterated design optimizations and real-time model-based control almost implausible.

There are also studies on fish swimming dynamics based on beam theories. The work in [18] presents a dynamics model based on the Euler-Bernoulli beam theory. However, the work assumes small deformations of the fish’s body (which is generally not the case during fish swimming) and prescribes the forward swimming speed as a constant. The work in [19] models the fishtail as a hinged beam and performs modal analysis on its linear vibrations. However, the work also assumes only small deformations; moreover, the limitation of flexibility to the tail part makes the model unable to capture anguilliform or subcarangiform swimming styles.

*Corresponding author: wwang745@wisc.edu.

Building on the preceding discussion, this letter presents a physics-grounded and fully interpretable model that captures the full-body dynamics of fish swimming. The model accounts for continuously distributed body elasticity with arbitrarily large deformations, incorporates both reactive and resistive hydrodynamic forces from the surrounding fluid, and enables self-propulsion without any imposed or prescribed kinematics. We further conduct a preliminary parameter study, investigating how swimming performance is influenced by actuation frequencies, body stiffness, and body length, thereby providing insights into both the fundamental dynamics of fish swimming and the design of efficient robotic swimmers.

II. KINEMATICAL OVERVIEW

As shown in Fig. 1, we model the robotic fish as a rigid head and an elastic body connected by a motor-driven revolute joint; this modeling scheme is also capable of capturing many other types of structures, such as the design where a wire-driven plate is placed at the connection between the head and the body, with the driving motor attached to the head [20]. Let $X_1Y_1Z_1$ be the inertial frame, attach $x_1y_1z_1$

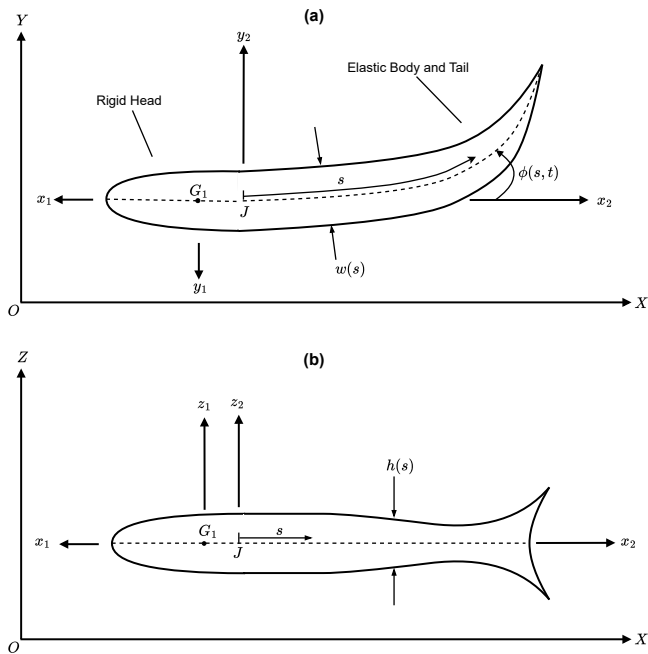


Fig. 1: Configuration and coordinate systems of the fish model; (a) top view and (b) side view of the fish.

to the center of mass (COM) G_1 of the fish's head, and attach $x_2y_2z_2$ to the joint connecting the head and the body, so that it rotates with the head. We model the cross-section of the fish body as an ellipse whose axis lengths $w(s)$ and $h(s)$ can vary along the body.

A. Generalized Coordinates and Displacement Fields

We focus on the planar maneuvers of the fish. Thus, we model the head of the fish as a rigid body described by 3 unconstrained generalized coordinates: X_{G_1} , Y_{G_1} , and θ_{G_1} .

We model the fish's body as Euler's elastica [21] that can go through large deformations in the x_2y_2 -plane. The tangential angle $\phi(s, t)$ describes the fish body's relative displacement field, where s denotes the Lagrangian coordinate along the fish body. Under this framework, we describe the rotation of the fish's body about the joint as a special deformation represented by the rigid-body mode (more detailed discussions in Section IV). To facilitate the following derivations, we also utilize the coordinates $x_2(s, t)$ and $y_2(s, t)$ for each point along the fish body. The coordinates are related to the displacement field $\phi(s, t)$ by the inextensibility condition, $(\frac{\partial x_2}{\partial s})^2 + (\frac{\partial y_2}{\partial s})^2 = 1$, and thus

$$x_2(s, t) = \int_0^s \cos(\phi(\sigma, t)) d\sigma \quad (1)$$

$$y_2(s, t) = \int_0^s \sin(\phi(\sigma, t)) d\sigma \quad (2)$$

B. Velocities and Accelerations

Accelerations are indispensable for computing hydrodynamic reactive forces, and thus we derive expressions for the accelerations of the fish's head and body in addition to the velocity expressions. Denote the rotation matrices of $x_1y_1z_1$ and $x_2y_2z_2$ as \mathbf{R}_{G_1} and \mathbf{R}_J . Denote the unit vectors of the inertial frame as $\{\hat{I}, \hat{J}, \hat{K}\}$ and the unit vectors of the head and joint frame as $\{\hat{i}_1, \hat{j}_1, \hat{k}_1\}$ and $\{\hat{i}_2, \hat{j}_2, \hat{k}_2\}$. We use the rotation matrices to express all unit vectors in the inertial frame. The velocity and acceleration of the head's COM can be written in the inertial frame as

$$\mathbf{v}_{G_1} = \dot{X}_{G_1} \hat{I} + \dot{Y}_{G_1} \hat{J} \quad (3)$$

$$\mathbf{a}_{G_1} = \ddot{X}_{G_1} \hat{I} + \ddot{Y}_{G_1} \hat{J} \quad (4)$$

The head's angular velocity $\boldsymbol{\omega}_{G_1}$ and angular acceleration $\boldsymbol{\alpha}_{G_1}$ are

$$\boldsymbol{\omega}_{G_1} = \dot{\theta}_{G_1} \hat{K}, \quad \boldsymbol{\alpha}_{G_1} = \ddot{\theta}_{G_1} \hat{K} \quad (5)$$

And the velocity of point J is

$$\mathbf{v}_J = \mathbf{v}_{G_1} + \boldsymbol{\omega}_{G_1} \times (-L_{G_1J} \hat{i}_1) \quad (6)$$

where L_{G_1J} denotes the distance from the head COM to the joint. The acceleration of point J is

$$\begin{aligned} \mathbf{a}_J = & \mathbf{a}_{G_1} + \boldsymbol{\alpha}_{G_1} \times (-L_{G_1J} \hat{i}_1) \\ & + \boldsymbol{\omega}_{G_1} \times (\boldsymbol{\omega}_{G_1} \times (-L_{G_1J} \hat{i}_1)) \end{aligned} \quad (7)$$

And thus the velocity of a point on the fish's body with Lagrangian coordinate s is

$$\mathbf{v}_s = \mathbf{v}_J + (\mathbf{v}_s)_{x_2y_2z_2} + \boldsymbol{\omega}_J \times \mathbf{r}_{s/J} \quad (8)$$

where $(\mathbf{v}_s)_{x_2y_2z_2} = \frac{\partial x_2}{\partial t} \hat{i}_2 + \frac{\partial y_2}{\partial t} \hat{j}_2$ is the velocity of the point as seen from $x_2y_2z_2$ and $\mathbf{r}_{s/J} = x_2 \hat{i} + y_2 \hat{j}$ denotes the relative position of the point with Lagrangian coordinate s to the joint. The acceleration of a point on the fish's body is

$$\begin{aligned} \mathbf{a}_s = & \mathbf{a}_J + (\mathbf{a}_s)_{x_2y_2z_2} + \underbrace{\boldsymbol{\alpha}_{G_1} \times \mathbf{r}_{s/J}}_{\text{tangential}} \\ & + \underbrace{\boldsymbol{\omega}_{G_1} \times (\boldsymbol{\omega}_{G_1} \times \mathbf{r}_{s/J})}_{\text{normal}} + \underbrace{2\boldsymbol{\omega}_{G_1} \times (\mathbf{v}_s)_{x_2y_2z_2}}_{\text{Coriolis}} \end{aligned} \quad (9)$$

where $(\mathbf{a}_s)_{x_2 y_2 z_2} = \frac{\partial^2 x_2}{\partial s^2} \hat{i}_2 + \frac{\partial^2 y_2}{\partial s^2} \hat{j}_2$ is the acceleration of the point as seen from $x_2 y_2 z_2$.

III. ENERGY FUNCTIONALS AND VIRTUAL WORK OF APPLIED FORCES

We derive the equations of motion of the fish based on Hamilton's principle (a.k.a. Hamilton's action principle), which states that

$$\int_{t_0}^{t_f} (\delta \mathcal{L} + \delta W) dt = 0 \quad (10)$$

where $\mathcal{L} = T - V$ is the Lagrangian of the system (T and V stand for kinetic and potential energies), δW stands for the virtual work done by forces that are not accounted for by potential energies, and the δ in front of \mathcal{L} is the variational operator.

A. Kinetic and Potential Energies

The kinetic energy of the rigid head, T_{head} , is

$$T_{\text{head}} = \frac{1}{2} m_1 v_{G_1}^2 + \frac{1}{2} I_{G_1} \omega_{G_1}^2 \quad (11)$$

where I_{G_1} is the moment of inertia of the head about its COM along z_1 . The kinetic energy of the fish's body is

$$T_{\text{body}} = \int_0^{L_2} \frac{1}{2} \rho(s) v_s^2 ds \quad (12)$$

where $\rho(s)$ is the linear density distribution of the fish body and L_2 is the length of the fish body. Then the total kinetic energy is $T = T_{\text{head}} + T_{\text{body}}$.

Since we focus on planar motions, only the body strain energy from elastic deformations contributes to the total potential energy; the potential energy can be written as

$$V = \int_0^{L_2} \frac{1}{2} E(s) I(s) \left(\frac{\partial \phi}{\partial s} \right)^2 ds \quad (13)$$

where $E(s)$ is the Young's modulus of elasticity and $I(s)$ is the second moment of area of the body's cross-section (i.e., EI is the bending rigidity of the fish's body), both of which can vary along the body as functions of the Lagrangian coordinate s .

B. Joint Motor Torque

Denote the motor torque as τ_m ; then the virtual work done by the motor torque and its reaction is

$$\begin{aligned} \delta W_m &= \tau_m \hat{k}_2 \cdot (\delta \vec{\theta}_{G_1} + \delta \vec{\phi}|_{s=0}) - \tau_m \hat{k}_1 \cdot \delta \vec{\theta}_{G_1} \\ &= \tau_m \hat{k}_2 \cdot \delta \vec{\phi}|_{s=0} = \tau_m \delta \phi|_{s=0} \end{aligned} \quad (14)$$

C. Water Reactive Force and Moment on the Head

Since the head is modeled as a rigid body, the water reactive force and moment on the head can be computed by the added mass matrix, $\mathbf{M}_a^{\text{head}}$:

$$\begin{bmatrix} \mathbf{F}_r^{\text{head}} \\ \tau_r^{\text{head}} \end{bmatrix} = - \begin{bmatrix} \mathbf{R}_{G_1} & 0 \\ 0 & 1 \end{bmatrix} \mathbf{M}_a^{\text{head}} \begin{bmatrix} \mathbf{R}_{G_1}^\top \mathbf{a}_{G_1} \\ \alpha_{G_1} \end{bmatrix} \quad (15)$$

where the head's geometry is approximate as an ellipsoid with added mass matrix obtained from [22]. Then the virtual work is given by

$$\delta W_r^{\text{head}} = \mathbf{F}_r^{\text{head}} \cdot \delta \mathbf{r}_{G_1} + \tau_r^{\text{head}} \delta \theta_{G_1} \quad (16)$$

D. Water Reactive Forces on the Body

Lighthill's large-amplitude elongated body theory provides an effective integral form of the fluid momentum balance for computing the total water reactive forces on the body [23]. However, since we are concerned about the full dynamics of the robotic fish rather than only the total thrust force given a prescribed motion, the original integral form does not suffice. Therefore, we extract the differential form of the fluid momentum balance to compute the load distribution along the fish's body.

Fig. 2 shows a differential control volume of the water added mass around the fish's body. The normal and tangential

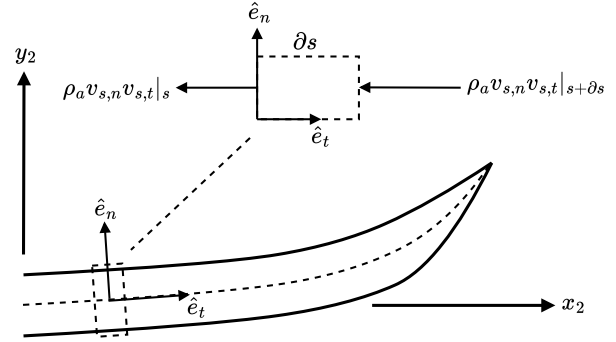


Fig. 2: Differential control volume and its momentum flux of the water added mass around the fish's body.

unit vectors can be written as

$$\hat{e}_t = \frac{\partial x_2}{\partial s} \hat{i}_2 + \frac{\partial y_2}{\partial s} \hat{j}_2 \quad (17)$$

$$\hat{e}_n = -\frac{\partial y_2}{\partial s} \hat{i}_2 + \frac{\partial x_2}{\partial s} \hat{j}_2 \quad (18)$$

According to Lighthill's large-amplitude elongated body theory, only the momentum in the normal direction (i.e., direction parallel to \hat{e}_n) is the dominant momentum in determining the water reactive forces. Denote \mathbf{p}_n as the normal directional momentum per unit length; then

$$\mathbf{p}_n = \rho_a v_{s,n} \hat{e}_n \quad (19)$$

where $v_{s,n} = \mathbf{v}_s \cdot \hat{e}_n$ is the normal velocity component of the point on the fish's body with Lagrangian coordinate s . Then the momentum balance of the differential control volume is

$$\frac{d}{dt} (\mathbf{p}_n) = \underbrace{\frac{\partial}{\partial s} (\rho_a v_{s,n} v_{s,t})}_{\text{convective flux}} \hat{e}_n - \underbrace{\frac{\partial}{\partial s} \left(\frac{1}{2} \rho_a v_{s,n}^2 \right)}_{\text{dynamic pressure}} \hat{e}_t - \underbrace{\mathbf{f}_r}_{\text{unknown}} \quad (20)$$

where $\rho_a = \frac{1}{4} \pi \rho_{\text{water}} h^2$ is the added mass per unit length (h is the depth of the cross-sectional area), \mathbf{f}_r is the water reactive force per unit length that the control volume applies to the fish body, and

$$\frac{d}{dt} (\mathbf{p}_n) = \rho_a \frac{\partial v_{s,n}}{\partial t} \hat{e}_n + \rho_a v_{s,n} (\boldsymbol{\omega}_{G_1} + \frac{\partial \phi}{\partial t} \hat{k}_2) \times \hat{e}_n \quad (21)$$

By equating Eq. (20) and Eq. (21), we can solve for the reactive force per unit length, \mathbf{f}_r . Then the virtual work of

water reactive forces on the fish's body is

$$\delta W_r^{\text{body}} = \int_0^{L_2} \mathbf{f}_r \cdot \delta \mathbf{r}_s ds \quad (22)$$

E. Water Drag Forces

Since the fish moves at relatively low speeds, the drag forces on the fish's head and body can be modeled as linear damping, and the forces and moments can be written as

$$\begin{bmatrix} \mathbf{F}_d^{\text{head}} \\ \tau_d^{\text{head}} \end{bmatrix} = - \begin{bmatrix} \mathbf{R}_{G_1} & 0 \\ 0 & 1 \end{bmatrix} \mathbf{D}^{\text{head}} \begin{bmatrix} \mathbf{R}_{G_1}^{\top} \mathbf{v}_{G_1} \\ \omega_{G_1} \end{bmatrix} \quad (23)$$

and

$$\mathbf{f}_d = -c_d \mathbf{v}_s \quad (24)$$

where \mathbf{D}^{head} is the drag matrix of the rigid head and c_d is the drag coefficient along the elastic body. The virtual work of drag forces is then

$$\delta W_d = \mathbf{F}_d^{\text{head}} \cdot \delta \mathbf{r}_{G_1} + \tau_d^{\text{head}} \delta \theta_{G_1} + \int_0^{L_2} \mathbf{f}_d \cdot \delta \mathbf{r}_s ds \quad (25)$$

IV. RITZ SERIES AND COMPUTATIONAL METHODS

Directly utilizing the derivations in Section III leads to integro-partial differential equations (integro-PDEs) that pose challenges to obtaining numerical solutions. To obtain equations of motion that can be readily solved numerically, we implement the Ritz series method, high-precision Gauss-Legendre quadrature, and forward-mode automatic differentiation (AD) [24] to obtain the projected weak form written as

$$\mathbf{M} \ddot{\mathbf{q}}^c = \mathbf{F} \quad (26)$$

where \mathbf{M} is the mass matrix, \mathbf{F} is the excitation vector, and \mathbf{q}^c is the vector containing all generalized coordinates of the robotic fish (i.e., the vector representing the full configuration space of the robotic fish given the Ritz series). Then we can compute the instantaneous generalized accelerations at any instant by solving the linear system represented as Eq. (26) using direct methods. The system trajectory can then be obtained using numerical integrators for solving ordinary differential equations (ODEs).

A. Ritz Series Approximations

We approximate the displacement field represented by the tangential angle $\phi(s, t)$ as

$$\phi(s, t) = \sum_{n=1}^N q_n(t) \psi_n(s) \quad (27)$$

where $\psi_n(s)$ are the Ritz basis functions (shape functions), $q_n(t)$ are the Ritz coefficients (generalized coordinates), and N is the total number of basis functions. It can be proven that as N increases, this approximation would yield a representation that converges to the true response [25].

Since the Ritz basis functions set the spatial dependencies, the energy expressions are reduced from functionals of the displacement field (and its spatial and temporal derivatives)

to functions of generalized coordinates (and their time derivatives). Specifically, the body coordinate x_2 can be written as

$$\begin{aligned} x_2(s, t) &= \int_0^s \cos \left(\sum_{n=1}^N q_n(t) \psi_n(\sigma) \right) d\sigma \\ &= x_2(s, q_1, \dots, q_N) \end{aligned} \quad (28)$$

And its temporal derivative, obtained using the chain rule, is

$$\begin{aligned} \frac{\partial x_2}{\partial t} &= \int_0^s - \left(\sum_{n=1}^N \dot{q}_n(t) \psi_n(\sigma) \right) \sin \left(\sum_{n=1}^N q_n(t) \psi_n(\sigma) \right) d\sigma \\ &= \dot{x}_2(s, q_1, \dots, q_N, \dot{q}_1, \dots, \dot{q}_N) \end{aligned} \quad (29)$$

where the dot above x_2 denotes a temporal derivative in a continuous system. The spatial derivative of x_2 can be written as

$$\begin{aligned} \frac{\partial x_2}{\partial s} &= \int_0^s - \left(\sum_{n=1}^N q_n(t) \psi'_n(\sigma) \right) \sin \left(\sum_{n=1}^N q_n(t) \psi_n(\sigma) \right) d\sigma \\ &= x'_2(s, q_1, \dots, q_N) \end{aligned} \quad (30)$$

where the prime symbol near x_2 and ψ_n denotes a spatial derivative in a continuous system. The coordinate y_2 and its spatial and temporal derivatives can be obtained similarly as functions of s , q_n 's, and time derivatives of q_n 's. Therefore, the energy functionals, which are integrals of x_2 , y_2 , and their spatial and temporal derivatives over the total length of the fish body, can then be represented as functions of q_n 's and their time derivatives.

Note that the integrals from Eq. (28) to Eq. (30) cannot be evaluated analytically for most basis function choices, and thus we numerically evaluate all the integrals using high-precision Gauss-Legendre quadrature. That is, we set up K Gauss-Legendre nodes along the fish body, and at each node, we evaluate x_2 , y_2 , and their derivatives at this node (these are the inner integrals); then we compute the kinematics (i.e., velocities, accelerations, and curvatures) at the K nodes using the inner integrals; finally, we compute the total kinetic and potential energies by the weighted Gauss-Legendre sum over the K nodes (these are the outer integrals).

B. Selections and Normalizations of Ritz Basis Functions

Under this Ritz series representation, a rigid-body mode, $\psi_1(s) = 1$ (i.e., constant-angle mode), must be included in the basis functions to represent the rotation of the fish body about the joint.

Other basis functions of the Ritz series need to be linearly independent and satisfy the geometric boundary condition at the joint, which is $\phi(0, t) = 0$. Therefore, we start with monomial basis functions in addition to the rigid-body mode to capture deformations of the fish body; that is:

$$\hat{\psi}_n(s) = s^{n-1}, \quad n = 1, 2, 3, \dots \quad (31)$$

To mitigate the ill-conditioning of the mass matrix and the numerical stiffness of the resulting ODEs, we normalize the

basis functions about the density distribution of the fish body. Specifically, we define the ρ -norm of a basis function as

$$\|\hat{\psi}_n\|_\rho = \sqrt{\langle \hat{\psi}_n, \hat{\psi}_n \rangle_\rho} \quad (32)$$

where $\langle \hat{\psi}_n, \hat{\psi}_n \rangle_\rho$ is the weighted inner product:

$$\langle \hat{\psi}_n, \hat{\psi}_n \rangle_\rho = \int_0^{L_2} \rho \hat{\psi}_n^2 ds \quad (33)$$

Then the basis functions to use are

$$\psi_n = \begin{cases} 1 & \text{if } n = 1 \\ \frac{\hat{\psi}_n}{\|\hat{\psi}_n\|_\rho} & \text{if } n > 1 \end{cases} \quad (34)$$

C. The Projected Weak Form

The Ritz series and Gauss-Legendre quadrature reduce Hamilton's principle for the system to Lagrange's equations. Specifically, let $\mathbf{q}^c = [X_{G_1} \ Y_{G_1} \ \theta_{G_1} \ q_1 \ \dots \ q_N]^\top$, and let q_j^c denote the j -th element in \mathbf{q}^c . With the displacement field written in Ritz series, the variation of the kinetic energy can be written as

$$\delta T(\mathbf{q}^c, \dot{\mathbf{q}}^c) = \sum_{j=1}^{N_q} \left(\frac{\partial T}{\partial q_j^c} \delta q_j^c + \frac{\partial T}{\partial \dot{q}_j^c} \delta \dot{q}_j^c \right) \quad (35)$$

Substituting it into the integration in Eq. (10) gives

$$\int_{t_0}^{t_f} \delta T dt = \sum_{j=1}^{N_q} \int_{t_0}^{t_f} \left(\frac{\partial T}{\partial q_j^c} \delta q_j^c + \frac{\partial T}{\partial \dot{q}_j^c} \delta \dot{q}_j^c \right) dt \quad (36)$$

Integration by parts converts the time derivative $\delta \dot{q}_j^c$ into δq_j^c :

$$\begin{aligned} \int_{t_0}^{t_f} \delta T dt &= \sum_{j=1}^{N_q} \int_{t_0}^{t_f} \left(\frac{\partial T}{\partial q_j^c} \delta q_j^c - \frac{d}{dt} \left(\frac{\partial T}{\partial \dot{q}_j^c} \right) \delta q_j^c \right) dt \\ &\quad + \underbrace{\frac{\partial T}{\partial \dot{q}_j^c} \delta q_j^c \big|_{t_0}^{t_f}}_0 \end{aligned} \quad (37)$$

The chain rule gives

$$\frac{d}{dt} \left(\frac{\partial T}{\partial \dot{q}_j^c} \right) = \sum_{k=1}^{N_q} \left(\frac{\partial^2 T}{\partial \dot{q}_j^c \partial \dot{q}_k^c} \ddot{q}_k^c + \frac{\partial^2 T}{\partial \dot{q}_j^c \partial q_k^c} \dot{q}_k^c \right) \quad (38)$$

Therefore,

$$\int_{t_0}^{t_f} \delta T dt = \int_{t_0}^{t_f} \left(\nabla_{\mathbf{q}^c} T - \frac{\partial^2 T}{\partial \dot{\mathbf{q}}^c \partial \dot{\mathbf{q}}^c} \ddot{\mathbf{q}}^c - \frac{\partial^2 T}{\partial \dot{\mathbf{q}}^c \partial \mathbf{q}^c} \dot{\mathbf{q}}^c \right)^\top \delta \mathbf{q}^c dt \quad (39)$$

where all the derivatives are evaluated via AD. Similarly,

$$\int_{t_0}^{t_f} \delta V dt = \int_{t_0}^{t_f} (\nabla_{\mathbf{q}^c} V)^\top \delta \mathbf{q}^c dt \quad (40)$$

We proceed to derive the projections of the forcing terms onto the generalized coordinates (i.e., the generalized forces given the Ritz series). Since

$$\delta \phi|_{s=0} = \sum_{n=1}^N \frac{\partial \phi_n}{\partial q_n} \delta q_n|_{s=0} = \frac{\partial \phi_1}{\partial q_1} \delta q_1 = \delta q_1 \quad (41)$$

then the generalized forces of the joint motor torque are

$$\mathbf{Q}_m = [0 \ 0 \ 0 \ \tau_m \ 0 \ \dots \ 0]^\top \quad (42)$$

Since the generalized coordinates of the head are chosen from fixed references, the generalized forces of the water reactive forces on the head are

$$\mathbf{Q}_r^{\text{head}} = \begin{bmatrix} -\mathbf{M}_a^{\text{head,eff}} & 0_{3 \times N} \\ 0_{N \times 3} & 0_{N \times N} \end{bmatrix} \ddot{\mathbf{q}}^c \quad (43)$$

where

$$\mathbf{M}_a^{\text{head,eff}} = \begin{bmatrix} \mathbf{R}_{G_1} & 0 \\ 0 & 1 \end{bmatrix} \mathbf{M}_a^{\text{head}} \begin{bmatrix} \mathbf{R}_{G_1}^\top & 0 \\ 0 & 1 \end{bmatrix} \quad (44)$$

Similarly, the generalized forces of water drag on the head can be written as

$$\mathbf{Q}_d^{\text{head}} = \begin{bmatrix} -\mathbf{D}_a^{\text{head,eff}} & 0_{3 \times N} \\ 0_{N \times 3} & 0_{N \times N} \end{bmatrix} \dot{\mathbf{q}}^c \quad (45)$$

where

$$\mathbf{D}_a^{\text{head,eff}} = \begin{bmatrix} \mathbf{R}_{G_1} & 0 \\ 0 & 1 \end{bmatrix} \mathbf{D}_a^{\text{head}} \begin{bmatrix} \mathbf{R}_{G_1}^\top & 0 \\ 0 & 1 \end{bmatrix} \quad (46)$$

Denote the Jacobian matrix at a Gauss-Legendre node as $\mathbf{J}_s = \frac{\partial \mathbf{r}_s}{\partial \mathbf{q}^c}$, then the virtual work done by the water reactive forces on the body is

$$\begin{aligned} \delta W_r^{\text{body}} &= \int_0^{L_2} \mathbf{f}_r^\top \delta \mathbf{r}_s ds = \int_0^{L_2} \mathbf{f}_r^\top \mathbf{J}_s^\top \mathbf{J}_s \delta \mathbf{q}^c ds \\ &= \left(\int_0^{L_2} \mathbf{J}_s^\top \mathbf{f}_r ds \right)^\top \delta \mathbf{q}^c \end{aligned} \quad (47)$$

Similarly, the virtual work done by the water drag on the body is

$$\delta W_d^{\text{body}} = \int_0^{L_2} \mathbf{f}_d^\top \delta \mathbf{r}_s ds = \left(\int_0^{L_2} \mathbf{J}_s^\top \mathbf{f}_d ds \right)^\top \delta \mathbf{q}^c \quad (48)$$

Substituting Eqs. (39), (40), (42), (43), (45), (47) and (48) into Eq. (10), the fundamental lemma of the calculus of variations yields the ODEs governing the motions of the robotic fish. Move all terms containing generalized accelerations to the left side of the ODEs to incorporate them into the mass matrix, and then we obtain the final projected weak form in Eq. (26), where

$$\mathbf{M} = \frac{\partial^2 T}{\partial \dot{\mathbf{q}}^c \partial \dot{\mathbf{q}}^c} + \begin{bmatrix} \mathbf{M}_a^{\text{head,eff}} & 0 \\ 0 & 0 \end{bmatrix} - \frac{\partial}{\partial \dot{\mathbf{q}}^c} \int_0^{L_2} \mathbf{J}_s^\top \mathbf{f}_r ds \quad (49)$$

and

$$\begin{aligned} \mathbf{F} &= \nabla_{\mathbf{q}^c} T - \frac{\partial^2 T}{\partial \dot{\mathbf{q}}^c \partial \dot{\mathbf{q}}^c} \ddot{\mathbf{q}}^c - \nabla_{\mathbf{q}^c} V + \mathbf{Q}_m + \mathbf{Q}_d^{\text{head}} \\ &\quad + \int_0^{L_2} \mathbf{J}_s^\top \mathbf{f}_r ds \Big|_{\dot{\mathbf{q}}^c=0} + \int_0^{L_2} \mathbf{J}_s^\top \mathbf{f}_d ds \end{aligned} \quad (50)$$

It is worth reiterating that all spatial integrals are evaluated using the Gauss-Legendre quadrature, and all derivatives (gradient, Hessian, and Jacobian computations) are evaluated using AD. The resulting ODEs can then be solved using numerical integrators that are accessible in most scientific

computing languages. Since the mass matrix \mathbf{M} is naturally ill-conditioned for this system given the strong coupling among the rigid head, the elastic body, and surrounding water, stiffness-aware methods (e.g., implicit methods) are needed for both efficiency and accuracy.

V. RESULTS

To validate our model and to provide insights on fish swimming and potential future design of robotic fish, we perform convergence experiments for the Ritz series and a preliminary design analysis based on numerical simulation results.

We implement our numerical simulations in Julia, using the ForwardDiff.jl package for automatic differentiations and the DifferentialEquations.jl package for numerical integrations [26]. We mainly use two stiffness-aware numerical integrators from the package - RadauIIA5 (a stable and accurate solver that implements the implicit Runge-Kutta method) and TRBDF2 (an efficient solver that combines the trapezoidal rule with the second-order backward difference formula). Our Julia code runs on a Dell G15 laptop with a 13th Gen Intel(R) Core(TM) i7-13650HX 2.60 GHz CPU and 16 GB RAM.

In the design analysis, we sweep over three parameters respectively - the tail-beat frequency, the baseline Young's modulus of elasticity of the fish's body, and the length of the fish's body, where the Young's modulus distribution is modeled as

$$E(s) = E_b - 0.7s^3 \cdot 10^6 \quad (51)$$

where E_b is the baseline Young's modulus. The amplitude of the joint motor oscillations is fixed at 0.4 rad (i.e., the joint motor sweeps over a range of 45.86°). We focus on two criteria for evaluating the propulsion performances of the robotic fish - the forward speed and the cost of transport (COT), defined as

$$\text{COT} = \frac{W_m}{m_{\text{total}}gd} \quad (52)$$

where W_m is the total work done by the joint motor, m_{total} is the total mass of the robotic fish, g is the gravitational acceleration, and d is the total distance travelled. Since the fish undulates as it moves forward, we use the displacement magnitude in the forward direction (i.e., X -direction) as the effective travelled distance. The COT serves as an important metric for evaluating the efficiency of propulsion during fish swimming. We use a PD controller on the joint angle to control the frequency and amplitude of the joint motor.

A. Convergence of Ritz Series

The correct number of Ritz basis functions (i.e., the number of terms used in the Ritz series) at which the system shows convergent behavior need to be chosen. We set the baseline Young's modulus to 0.35 MPa, a typical Young's modulus for bio-based soft materials [27]; we also set the tail-beat frequency to 2 Hz and joint motor amplitude to 0.4 rad (i.e., the joint motor sweeps over a range of 45.86°).

We increase the number of Ritz basis functions from 1 to 6, and compare the simulated trajectories over 3 full tail-beats (i.e., 1.5 s) from rest and the time consumed by the numerical simulations. The comparisons are shown in Fig. 3. From Fig.

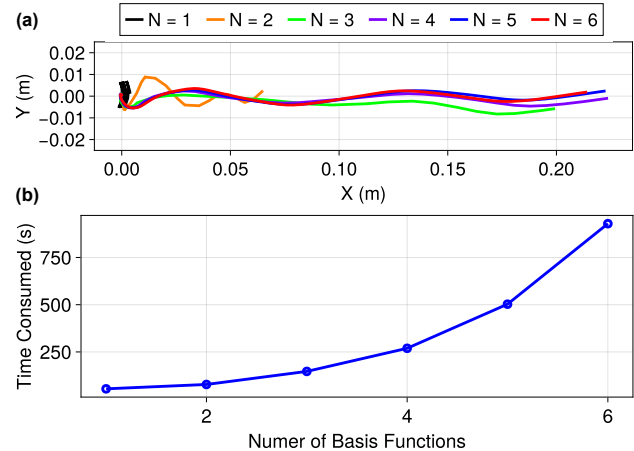


Fig. 3: (a) Comparisons of the fish head's COM trajectories over 3 full tail-beats, with the number of Ritz basis functions N increasing from 1 to 6; (b) times consumed by the numerical simulations as N increases.

3(a), it can be observed that the numerical simulation starts to show convergent behavior at $N = 4$, and the trajectories of the fish head's COM at $N = 5$ and $N = 6$ are very close to one another. Considering the amount of time consumed by the simulation when $N = 6$, as shown in Fig. 3(b), we pick $N = 5$ for the rest of the numerical experiments as a balance between accuracy and computational efficiency.

B. Parameter Sweep over Tail-Beat Frequency

We fix the body length to 0.3 m and the baseline Young's modulus to 0.35 MPa. We then perform a parameter sweep for the tail-beat frequency, ranging from 0.5 Hz to 3.5 Hz with an interval of 0.5 Hz; the results are shown in Fig. 4. It can be observed from Fig. 4 that the steady-state forward speed peaks at a tail-beat frequency of 3 Hz, while the COT is minimized at a tail-beat frequency of 1 Hz.

C. Parameter Sweep over Baseline Young's Modulus

We fix the body length to 0.3 m and the tail-beat frequency to 2 Hz. Then we perform a parameter sweep for the baseline Young's modulus of the fish's body, ranging from 0.2 MPa to 0.5 MPa with an interval of 0.05 MPa; the results are shown in Fig. 5. From Fig. 5, the forward speed is optimized at 0.25 MPa and COT is optimized at 0.3 MPa.

D. Parameter Sweep over Body Length

We fix the body Young's modulus to 0.35 MPa and the tail-beat frequency to 2 Hz. Then we perform a parameter sweep on the length of the fish's body, ranging from 0.25 m to 0.45 m with an interval of 0.05 m; the results are shown in Fig. 6. It can be observed from Fig. 6 that both the forward speed and the COT are optimized at a body length of 0.35 m.

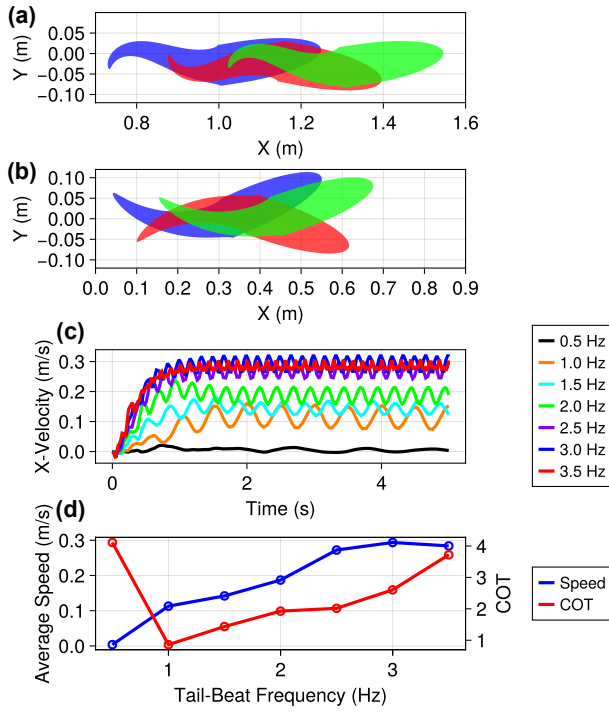


Fig. 4: Simulation results of the tail-beat frequency sweep. Time-lapse plot of the fish from $t = 4s$ to $t = 5s$ with a tail-beat frequency of (a) 3 Hz and (b) 1 Hz (blue-red-green sequence); (c) X -direction velocity plots and (d) plots of steady-state average speed and COT at different tail-beat frequencies.

VI. DISCUSSION

From the numerical experiments, we observe that varying the tail-beat frequency has the most impact on both steady-state speed and the COT. However, the optimal frequencies for speed and COT do not occur simultaneously - for a tail-beat frequency of ≥ 1 Hz, increasing the steady-state speed results in an increase in COT (which implies a decrease in propulsion efficiency), and vice versa. Therefore, trade-offs need to be made and priorities need to be taken.

It is also interesting to observe the non-convex COT distribution during the parameter sweep on the baseline Young's modulus of the fish's body. It could be a future direction of study to see if this shape holds for all neighboring tail-beat frequencies and body lengths. It is also important to note that, though varying the baseline Young's modulus at the range of 0.2 MPa to 0.5 MPa has limited impact on both the steady-state speed and the COT, this does not imply that the impact of the Young's modulus distribution throughout the fish's body is trivial - in our numerical experiments, we assume that the Young's modulus distribution takes the form of Eq. (51) and vary only the value of E_b ; however, the elasticity distribution can in fact be more sophisticated and involve more terms (and our dynamics model and Julia-based simulation code can readily adapt to that by changing a single line of function definition), and thus more study can be done on the elasticity distribution part as well.

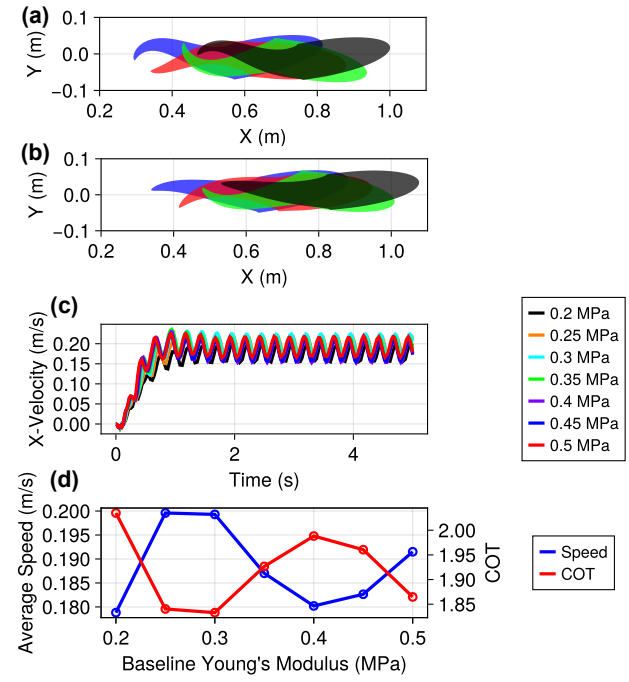


Fig. 5: Simulation results of the baseline Young's modulus sweep. Time-lapse plot of the fish from $t = 4s$ to $t = 5s$ with a baseline Young's modulus of (a) 0.2 MPa and (b) 0.35 MPa (blue-red-green-black sequence); (c) X -direction velocity plots and (d) plots of steady-state average speed and COT at different baseline Young's moduli.

The parameter sweep on the body length implies that keep increasing the body length is not necessarily beneficial for either speed or efficiency. Although one can obtain more total thrust since a longer body can provide a larger added mass in total, the long body can also bring more burdens since it has more total mass and drag. Moreover, the optimal body stiffness distributions at different body lengths can vary significantly, which is worth investigating in further parameter studies.

Throughout our design analysis, we have been sweeping over parameters of interest respectively. Although this method can provide us with preliminary insights on fish swimming and potential design of robotic fish, the optimizations are not performed in the full parameter space. In addition, our current parameter-sweep method does not fully utilize the automatically differentiable characteristic of our dynamics model. Therefore, an important next step is to utilize the differentiability of our model and implement numerical optimization algorithms, such as gradient descent and quasi-Newton methods, to optimize propulsion performances.

VII. CONCLUSION AND FUTURE WORK

To conclude, our work presents a physics-grounded and interpretable model for the full-body dynamics of fish swimming. Our model captures the dynamics of the distributed elasticity of the fish body under large deformations, while also incorporating reactive and resistive hydrodynamic

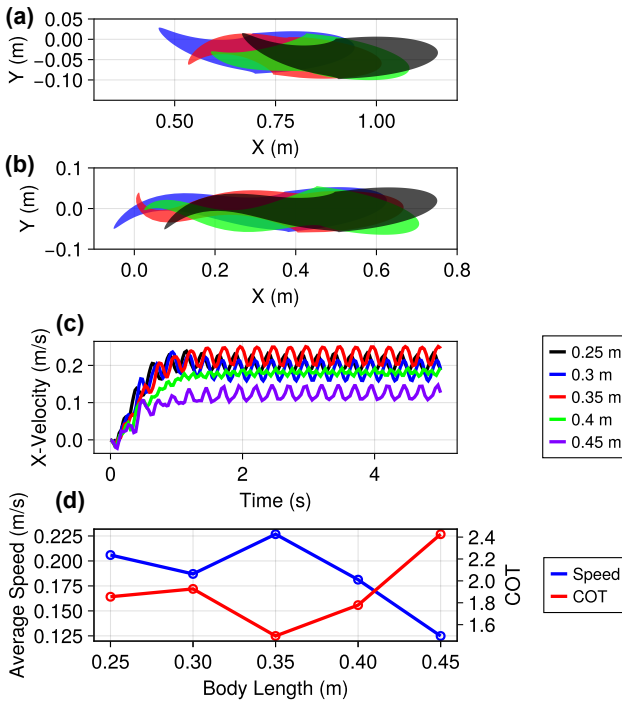


Fig. 6: Simulation results of the body length sweep. Time-lapse plot of the fish from $t = 4s$ to $t = 5s$ with a body length of (a) 0.25 m and (b) 0.45 m (blue-red-green-black sequence); (c) X -direction velocity plots and (d) plots of steady-state average speed and COT at different body lengths.

forces, offering a continuous and computationally tractable alternative to multi-segment, CFD, or FSI-based approaches. A preliminary parameter study on how actuation frequency, body stiffness, and body length affect speed and propulsion frequency offers key insights into biological swimming and the design of robotic swimmers.

Our future work includes utilizing the automatically differentiability of our dynamics model to perform high-dimensional numerical optimizations over the full parameter space to find the optimal geometries and material properties for maximizing swimming speed and efficiency. Moreover, we are interested in further model reductions to enable real-time model-based controls with hardware implementations on a robotic fish.

REFERENCES

- [1] G. Li, G. Liu, D. Leng, X. Fang, G. Li, and W. Wang, "Underwater undulating propulsion biomimetic robots: A review," *Biomimetics*, vol. 8, no. 3, p. 318, 2023.
- [2] T. Liu, Y. Liu, R. Zeng, B. Gan, M. Zhang, H. Li, S. Qu, and H. Zhou, "A bioinspired multimotion modality underwater microrobot," *Science Advances*, vol. 11, no. 19, p. eadu2527, 2025.
- [3] K. Iguchi, T. Shimooka, S. Uchikai, Y. Konno, H. Tanaka, Y. Ikemoto, and J. Shintake, "Agile robotic fish based on direct drive of continuum body," *npj Robotics*, vol. 2, no. 1, p. 7, 2024.
- [4] S. C. Van Den Berg, R. B. Scharff, Z. Rusák, and J. Wu, "Openfish: Biomimetic design of a soft robotic fish for high speed locomotion," *HardwareX*, vol. 12, p. e00320, 2022.
- [5] D. Quinn and G. Lauder, "Tunable stiffness in fish robotics: mechanisms and advantages," *Bioinspiration & Biomimetics*, vol. 17, no. 1, p. 011002, 2021.
- [6] L. Li, C. Wang, and G. Xie, "Modeling of a carangiform-like robotic fish for both forward and backward swimming: Based on the fixed point," in *2014 IEEE International Conference on Robotics and Automation (ICRA)*. IEEE, 2014, pp. 800–805.
- [7] X. Zheng, M. Xiong, R. Tian, J. Zheng, M. Wang, and G. Xie, "Three-dimensional dynamic modeling and motion analysis of a fin-actuated robot," *IEEE/ASME Transactions on Mechatronics*, vol. 27, no. 4, pp. 1990–1997, 2022.
- [8] G. Ozmen Koca, C. Bal, D. Korkmaz, M. C. Bingol, M. Ay, Z. H. Akpolat, and S. Yetkin, "Three-dimensional modeling of a robotic fish based on real carp locomotion," *Applied Sciences*, vol. 8, no. 2, p. 180, 2018.
- [9] J. Wang, P. K. McKinley, and X. Tan, "Dynamic modeling of robotic fish with a base-actuated flexible tail," *Journal of dynamic systems, measurement, and control*, vol. 137, no. 1, p. 011004, 2015.
- [10] X. Liao, C. Zhou, Q. Zou, J. Wang, and B. Lu, "Dynamic modeling and performance analysis for a wire-driven elastic robotic fish," *IEEE Robotics and Automation Letters*, vol. 7, no. 4, pp. 11174–11181, 2022.
- [11] H. Jiang and Y. Liu, "Nonlinear analysis of compliant robotic fish locomotion," *Journal of Vibration and Control*, vol. 28, no. 13-14, pp. 1673–1685, 2022.
- [12] T. McMillen and P. Holmes, "An elastic rod model for anguilliform swimming," *Journal of mathematical biology*, vol. 53, no. 5, pp. 843–886, 2006.
- [13] M. Curatolo and L. Teresi, "Modeling and simulation of fish swimming with active muscles," *Journal of theoretical biology*, vol. 409, pp. 18–26, 2016.
- [14] S.-I. Sohn, "A computational model of the swimming dynamics of a fish-like body in two dimensions," *Physics of Fluids*, vol. 33, no. 12, 2021.
- [15] Y. Lu, H. Zhang, D. Xu, and W.-X. Huang, "Nonlinear tunable stiffness for high-efficiency biomimetic propulsion," *Journal of Fluid Mechanics*, vol. 1017, p. A7, 2025.
- [16] J. O'Connor and B. D. Rogers, "A fluid–structure interaction model for free-surface flows and flexible structures using smoothed particle hydrodynamics on a gpu," *Journal of Fluids and Structures*, vol. 104, p. 103312, 2021.
- [17] W. Wu, C. Bonneville, and C. Earls, "A principled approach to design using high fidelity fluid-structure interaction simulations," *Finite Elements in Analysis and Design*, vol. 194, p. 103562, Oct. 2021. [Online]. Available: <http://dx.doi.org/10.1016/j.finel.2021.103562>
- [18] J.-Y. Cheng, T. Pedley, and J. Altringham, "A continuous dynamic beam model for swimming fish," *Philosophical Transactions of the Royal Society of London. Series B: Biological Sciences*, vol. 353, no. 1371, pp. 981–997, 1998.
- [19] V. Kopman and M. Porfiri, "Design, modeling, and characterization of a miniature robotic fish for research and education in biomimetics and bioinspiration," *IEEE/ASME Transactions on mechatronics*, vol. 18, no. 2, pp. 471–483, 2012.
- [20] A. Mazumdar, P. V. Y. Alvarado, and K. Youcef-Toumi, "Maneuverability of a robotic tuna with compliant body," in *2008 IEEE International Conference on Robotics and Automation*. IEEE, 2008, pp. 683–688.
- [21] R. E. Caflisch and J. H. Maddocks, "Nonlinear dynamical theory of the elastica," *Proceedings of the Royal Society of Edinburgh Section A: Mathematics*, vol. 99, no. 1-2, pp. 1–23, 1984.
- [22] J. N. Newman, *Marine hydrodynamics*. The MIT press, 2018.
- [23] M. J. Lighthill, "Large-amplitude elongated-body theory of fish locomotion," *Proceedings of the Royal Society of London. Series B. Biological Sciences*, vol. 179, no. 1055, pp. 125–138, 1971.
- [24] J. Revels, M. Lubin, and T. Papamarkou, "Forward-mode automatic differentiation in Julia," *arXiv:1607.07892 [cs.MS]*, 2016. [Online]. Available: <https://arxiv.org/abs/1607.07892>
- [25] J. Ginsberg, *Engineering dynamics*. Cambridge University Press, 2008, vol. 10.
- [26] C. Rackauckas and Q. Nie, "DifferentialEquations.jl—a performant and feature-rich ecosystem for solving differential equations in Julia," *Journal of Open Research Software*, vol. 5, no. 1, 2017.
- [27] Z. Cui, W. Wang, L. Guo, Z. Liu, P. Cai, Y. Cui, T. Wang, C. Wang, M. Zhu, Y. Zhou *et al.*, "Haptically quantifying young's modulus of soft materials using a self-locked stretchable strain sensor," *Advanced Materials*, vol. 34, no. 25, p. 2104078, 2022.